Article

Valorisation of Alkali–Thermal Activated Red Mud for High-Performance Geopolymer: Performance Evaluation and Environmental Effects

Zhiping Li *, Haifeng Dong, Yuwen Wang, Jianbing Men, Junqiang Wang, Xiushao Zhao, Sikai Zou

Posted Date: 11 July 2025

doi: 10.20944/preprints202507.0800.v1

Keywords: Low-carbon building materials; Red mud; Economic analysis; Compressive strength; waste management

Article

Valorisation of Alkali–Thermal Activated Red Mud for High-Performance Geopolymer: Performance Evaluation and Environmental Effects

Zhiping Li [1,2,*], Haifeng Dong [2], Yuwen Wang [2], Jianbing Men [3], Junqiang Wang [2], Xiushao Zhao [1,2] and Sikai Zou [1,2]

[1] State Key Laboratory of Safety and Resilience of Civil Engineering in Mountain Area, East China Jiaotong University, Nanchang 330013, China
[2] School of Civil Engineering and Architecture, East China Jiaotong University, Nanchang 330013, China
[3] China Nerin Engineering Co., Ltd., Nanchang, Jiangxi 330031, China
* Correspondence: lizhiping@ecjtu.edu.cn

Abstract

This study investigates the influence of SiO_2/Al_2O_3 molar ratios (2.25–3.00) and the replacement of red mud (RM) with GGBS (50–63%) on the performance of RM-based geopolymers to address the environmental issues posed by RM, including its high alkalinity and heavy metal content. The results indicated that increasing the SiO_2/Al_2O_3 ratio and incorporating GGBS reduced the fresh properties of the geopolymers. A higher SiO_2/Al_2O_3 ratio promoted the development of compressive strength, likely due to the elevated concentration of soluble silicates. The RM-based geopolymers with higher GGBS content also exhibited greater compressive strength. Moreover, the drying shrinkage and water permeability of RM-based geopolymers increased as the SiO_2/Al_2O_3 ratio and the GGBS content increased. The sustainability assessment revealed that CO_2 emissions were influenced by the SiO_2/Al_2O_3 ratio. In comparison to other RM-based geopolymers, the CO_2 emissions and costs in this study were reduced by 13.13%–44.33% and 3.64%–39.68%, respectively. This study discusses the effects of the SiO_2/Al_2O_3 molar ratios on the reaction process and strength formation mechanism of RM-based geopolymers, which provides an effective strategy for the resource utilization of RM.

Keywords: low-carbon building materials; red mud; economic Analysis; compressive strength; waste management

1. Introduction

The environmental impact of carbon dioxide (CO_2) emissions from Ordinary Portland Cement (OPC) production has driven increased research into alternative materials that can effectively replace OPC. [1,2]. Geopolymers, which consist of a framework structure formed by the condensation of tetrahedral silicoaluminate units, have emerged as a promising alternative [3]. They have gained wide attention in sustainable building materials due to their high early strength, chemical corrosion resistance, heat resistance, and durability [4]. Geopolymers are typically synthesized using alkaline solutions to activate aluminosilicate materials, including ground granulated blast furnace slag (GGBS) [5], fly ash (FA) [6], silica fume (SF) [7], metakaolin (MK) [8], coal gangue (CG) and rice husk ash (RHA) [9,10], etc. Compared to OPC, geopolymer production reduces energy consumption and CO_2 emissions by approximately 50% and 80%, respectively [11,12]. However, the growing attention to the resource value of GGBS, FA and SF has led to higher production costs, market prices and increased consumption of these materials. Therefore, it is necessary to explore alternative materials.

Red mud (RM) is an industrial solid waste commonly used as a precursor material in geopolymers for various civil engineering applications [13]. RM is a highly alkaline by-product (pH 10–13) generated during alumina production [14,15]. Additionally, Al_2O_3, SiO_2, and Na_2O are the

doi:10.20944/preprints202507.0800.v1

primary components of RM, which can be employed as precursors for geopolymer synthesis [16,17]. It serves as an alkali source and can be utilized as a precursor. Zakira et al. [18] developed high-performance RM-based geopolymers using a high proportion of RM and silica fume. The compressive strengths reached 61.2 MPa at 3 days and 65.7 MPa at 28 days, respectively. Tian et al. [19] observed that higher RM content tended to improve compressive strength and stiffness. Nikbin et al. [20] produced high-performance RM-based geopolymers and found that both the mechanical performance and elastic modulus decreased as RM content increased. The dissolution of RM or aluminosilicate is crucial in controlling the physical and mechanical properties of geopolymers [21–23]. Therefore, the research on the preparation of geopolymer cementitious materials using RM has garnered widespread attention.

The performance of geopolymers is affected by changes in their initial molar ratios, particularly those of SiO_2/Al_2O_3, Na_2O/Al_2O_3, and H_2O/Na_2O [24–26]. Several researchers have demonstrated the significance of the SiO_2/Al_2O_3 ratio in influencing the mechanical properties and microstructural of geopolymers [5,27]. Higher compressive strength has been observed in geopolymers with an SiO_2/Al_2O_3 ratio of around 2 and a Na_2O/Al_2O_3 ratio between 0.38 and 1.43 [28,29]. Rowles et al. [30] reported a peak compressive strength of 64 ± 3 MPa at a SiO_2/Al_2O_3 ratio of 2.5, while Kim et al. [31] demonstrated that geopolymer activated with NaOH and a Si/Al ratio of 3.0 achieved the highest strength due to stable Si–O–T bonds. However, strength tends to decrease when the SiO_2/Al_2O_3 ratio exceeds a certain value [32]. Zheng et al. [27] observed that FA-based geopolymers with intermediate SiO_2/Al_2O_3 ratios achieved the best compressive strength. Duxson et al. [33] pointed out that the SiO_2/Al_2O_3 ratios as crucial parameters influencing geopolymerization. In addition, the Na_2O/Al_2O_3 and H_2O/Na_2O ratios are vital for successful geopolymer synthesis [34]. Davidovits et al. [35] suggested optimal ranges of 0.8–1.6 for Na_2O/Al_2O_3 and 10–25 for H_2O/Na_2O to ensure high strength and durability. Therefore, assessing the mechanical properties of RM-based geopolymers according to their initial molar ratios is more appropriate, as these ratios have a greater influence than other factors such as NaOH solution concentration, water/binder ratio, and alkaline activator liquid to binder ratio [36]. Further investigation into how different initial molar ratios affect the properties of RM-based geopolymers is necessary.

This study investigated the influence of initial molar ratios (SiO_2/Al_2O_3, Na_2O/Al_2O_3, and H_2O/Na_2O) on the fresh and mechanical properties of RM-based geopolymers. Firstly, the SiO_2/Al_2O_3 ratio was varied while keeping the Na_2O/Al_2O_3 and H_2O/Na_2O ratios constant, with GGBS added to improve the performance of RM-based geopolymers. Subsequently, the flowability, setting time, compressive strength, drying shrinkage and water permeability were evaluated to develop high-performance geopolymers. The reaction mechanism and products were analyzed using XRD, FTIR, TG-DTG and SEM-EDS techniques. Finally, the CO_2 emissions and costs of RM-based geopolymers with varying SiO_2/Al_2O_3 ratios were studied and compared with other geopolymers containing RM and GGBS.

2. Experimental Program

2.1. Raw Materials

The RM and GGBS employed in this study were provided by Lingshou Mineral Products Co., Ltd., China. Their chemical compositions were listed in Table 1. RM was identified as an alkaline aluminosilicate material, with SiO_2/Al_2O_3 and Na_2O/Al_2O_3 molar ratios of 1.15 and 0.91, respectively. The particle morphological of RM and GGBS were shown in Figure 1. The thermal treatment for RM was fixed at 800°C according to previous studies [37]. Figure 2 shows the particle size distribution of RM and GGBS, as determined using a laser particle size analyser, and the volume median diameters (D_{50}) of RM and GGBS were 2.76 μm and 10.15 μm, respectively.

The alkaline activators consisted of industrial-grade sodium silicate ($Na_2O{\cdot}nSiO_2$) and analytical-grade sodium hydroxide (NaOH). The $Na_2O{\bullet}nSiO_2$ solution, supplied by Henan Borun Casting Materials Co., Ltd., had a chemical composition of 31.4% SiO_2, 11.9% Na_2O, and 56.7% H_2O. The solution's modulus and density were 2.68 and 1.485 g/mL, respectively. The NaOH powders, purchased from Guangdong Xilong Chemical Co., Ltd., had a purity greater than 96.0%.

Table 1. Chemical composition (wt%) of RM and GGBS.

Raw material	Al_2O_3	SiO_2	CaO	Na_2O	Fe_2O_3	TiO_2	Others	LOI
RM	25.11	16.93	6.02	11.60	36.43	1.54	1.70	-
GGBS	13.70	31.10	40.90	0.38	0.65	1.26	2.85	0.96

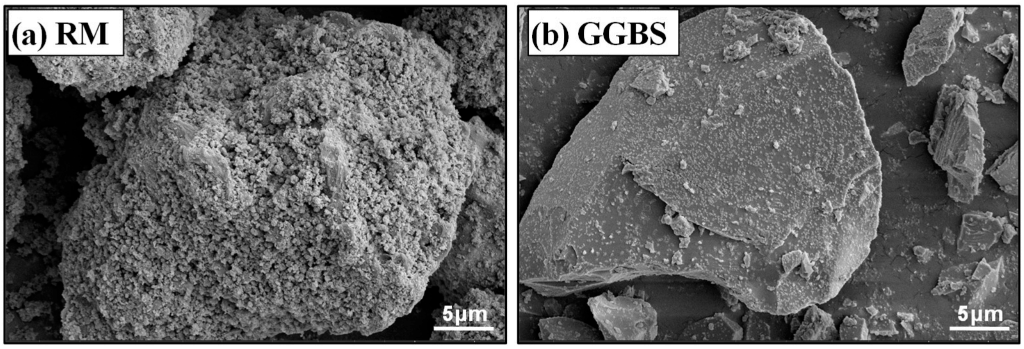

Figure 1. SEM images of RM and GGBS.

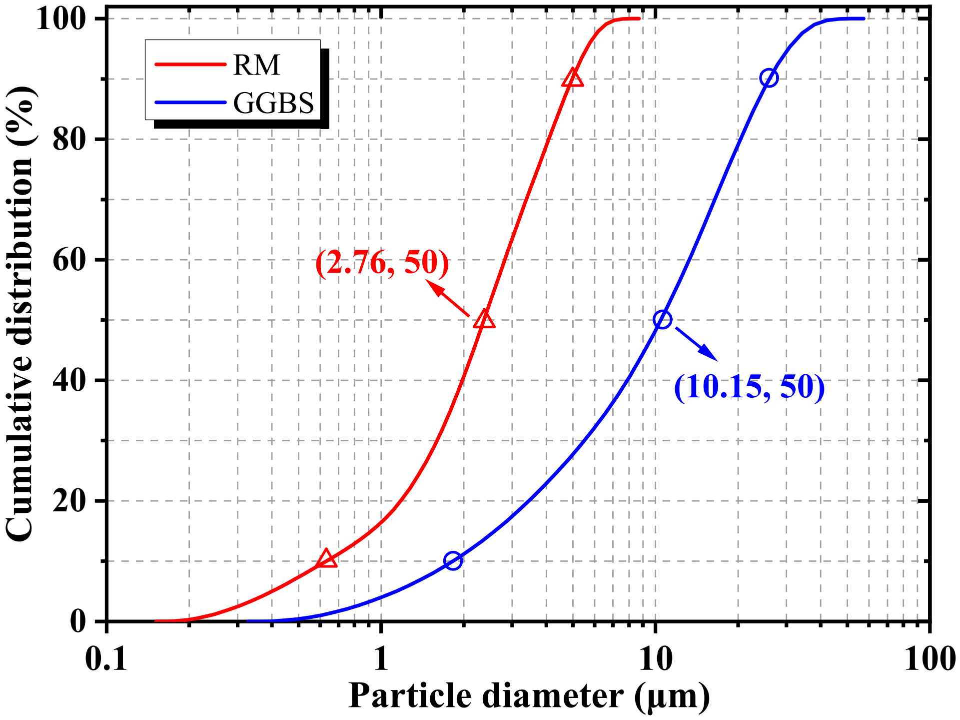

Figure 2. Particle size distribution of RM and GGBS.

2.2. Material Design and Preparation

Table 2 presents the classification of the mixtures into two groups. Group 1 was designed to explore the effect of the SiO_2/Al_2O_3 ratio while keeping the Na_2O/Al_2O_3 and H_2O/Na_2O ratios constant. Group 2 focused on evaluating the influence of replacing RM with GGBS, regardless of changes in the overall molar ratios. In this group, the water-to-binder (w/b) ratio was fixed at 0.5, and the Na_2O/precursor ratio was set at 0.04 to eliminate the their impact on the performance of the geopolymer. The w/b ratio was determined based on the total water content, including the water contained in $Na_2O{\bullet}nSiO_2$ solution and any additional water added. The proportions of the alkaline activator and RM-GGBS mixtures were adjusted according to the chemical compositions of the raw materials to achieve SiO_2/Al_2O_3 ratios ranging from 2.25 to 3.12 and Na_2O/Al_2O_3 ratios between 0.85 and 0.92. The alkaline activator mixture, composed of NaOH powder and $Na_2O•nSiO_2$ solution, was diluted with deionized water to achieve an H_2O/Na_2O molar ratios of 17.24.

Table 2. Mix proportions of thermally-activated RM–based geopolymers (wt%).

No.	Precursors		Activators [a]		SiO_2/Al_2O_3	Na_2O/Al_2O_3	H_2O/Na_2O	Water [a]	Remarks
	RM	GGBS	NaOH	$Na_2O·nSiO_2$					
Si300	36	64	0.035	0.074	3.00	0.85	17.24	0.363	Group 1
Si275	43	57	0.032	0.069	2.75	0.85	17.24	0.390	
Si256	50	50	0.026	0.072	2.56	0.85	17.24	0.406	
Si225	56	44	0.031	0.048	2.25	0.85	17.24	0.457	
GBS50	50	50	0.026	0.072	2.56	0.85	17.24	0.406	Group 2
GBS54	46	54	0.029	0.080	2.72	0.87	17.24	0.395	
GBS58	42	58	0.032	0.088	2.90	0.89	17.24	0.385	
GBS63	37	63	0.035	0.098	3.12	0.92	17.24	0.372	

a Relative to the total mass of the precursors.

Figure 3 illustrates the preparation process and experimental setup for RM-based geopolymers. RM and GGBS were mixed for 60 seconds using a laboratory-type JJ-5 cement mortar mixer. The alkaline activator was prepared by thoroughly mixing NaOH powder, $Na_2O·nSiO_2$ solution and deionized water, which was then sealed and cooled to room temperature. The mixing process began by adding the blended powders to the mixing bowl, followed by the addition of the alkaline solution, ensuring thorough mixing to obtain a uniform paste. The fresh geopolymer paste was then poured into cubic molds with dimensions of 40 mm × 40 mm × 40 mm. Subsequently, the filled molds were placed on a vibration table for approximately 60 seconds to eliminate trapped air and were covered with plastic film to prevent moisture loss. Specimens were left at ambient temperature for 24 hours. After demolding, all samples were transferred to a standard curing room maintained at 20 ± 2°C and over 95% relative humidity, where they were cured for the specified periods of 3, 7, 28, and 56 days.

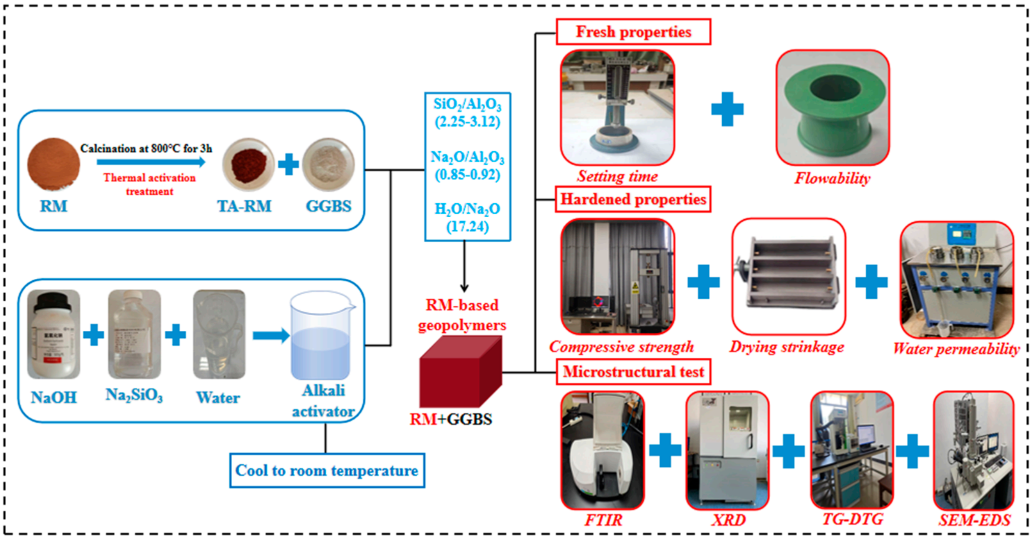

Figure 3. Procedure of the RM-based geopolymers preparation and the experiments.

2.3. Testing Methods

2.3.1. Flowability

The stirred RM-based geopolymer paste was poured into a truncated cone mold set on a flat glass plate. The conical mold had a height of 60 mm, with top and bottom diameters of 36 mm and 60 mm, respectively. The surface of the mold was leveled using a scraper, followed by starting the timer and vertically lifting the mold. After approximately 30 seconds, the maximum flow diameters of the geopolymer paste were measured in two perpendicular directions, and the average of these measurements was recorded as the flowability of RM-based geopolymers.

2.3.2. Setting Time

The RM-based geopolymer paste was cast into a frustum-shaped mold featuring an upper diameter of 65 mm, a lower inner diameter of 75 mm, and a height of 40 mm. The initial setting time of the RM-based geopolymers was determined 30 minutes after preparation, under standard curing conditions. The Vicat instrument was used, and it revealed that the geopolymer paste attained its initial setting phase when the test needle fell to a distance of 4 mm ± 1 mm from the glass surface. After the initial setting time was measured, the molds were removed from the glass plate, inverted by 180° with the larger diameter facing upwards, and placed back on the glass plate. The final setting time was recorded at 5-minute intervals, and the endpoint was identified when the test needle no longer produced visible impressions on the bottom surface of the specimen.

2.3.3. Compressive Strength

The prepared paste was poured into cubic molds measuring 40 mm × 40 mm × 40 mm molds, sealed with plastic wrap, and then cured for 3, 7, 28, and 56 days. Subsequently, the compressive strength of the RM-based geopolymers was evaluated at each curing time. Compressive strength tests were conducted using a WDW-10C 10-ton universal testing machine. The loading rate was maintained at 2.4 kN/s, and the average compressive strength was calculated based on three specimens per group.

2.3.4. Drying Shrinkage

Drying shrinkage samples were cast into molds measuring 25 mm × 25 mm × 280 mm, with copper nail heads pre-inserted at both ends, The molds were then cured at a constant temperature of 20 ± 1 ℃ for 24 hours. For each mix proportion, three samples were produced. The samples were then placed in a dry curing chamber maintained at controlled conditions (20 ± 2°C, relative humidity 50 ± 4%) for a predetermined period. The dimensional variation of each RM-based geopolymer specimen was accurately determined using a micrometer and length comparator.

2.3.5. Water Permeability

For the water permeability test, samples were cast in molds with dimensions of 175 mm (top diameter), 185 mm (bottom diameter), and 150 mm (height). Three samples were prepared for each group. The RM-based geopolymers were sealed with paraffin containing a small amount of rosin, placed into the test molds of the apparatus, and the sealing was checked before starting the test. The initial test pressure was maintained at 0.2 MPa for 1 hour, Subsequently, the pressure was increased incrementally by 0.1 MPa per hour until water seepage was observed, and the seepage height was recorded. If no seepage was observed on the top surface after 1 hour under 1.5 MPa pressure, the specimens were broken to measure the penetration depth of water.

2.3.6. SEM-EDS Analysis

After the compressive strength test, samples were taken from the middle section, immersed in anhydrous ethanol to leach unbound mixing water, and then oven-dried at 60 ℃ for 48 hours. The

doi:10.20944/preprints202507.0800.v1

microstructures of RM-based geopolymers were examined using a Apreo 2C SEM, and then elemental analysis was performed. After drying, the samples were fixed onto conductive tape and sputter-coated with a thin gold layer for 45 seconds to improve conductivity. The acceleration voltage was set to 10 kV for morphological imaging and 15 kV for energy spectrum mapping, using a secondary electron (SE) detector.

2.3.7. FTIR Analysis

The dried samples were ground and passed through an 80 μm sieve for microscopic analysis. The precursor powder was thoroughly blended with KBr at a mass ratio of 1:100. The composite powder was pelletized in a 13 mm to form a transparent pellet. FTIR spectra were measured using a PerkinElmer Spectrum 2 spectrometer in the range of 450 to 3,900 cm^{-1}, with a resolution of 4 cm^{-1}, performing a total of 32 scans to enhance data accuracy and reliability.

2.3.8. XRD Analysis

XRD analysis was performed to characterize the mineralogical properties of RM-based geopolymers. Prior to testing, samples were dried and ground to a particle size below 80 μm. The trough was filled with 2 g of powder and flattened using a glass plate. Subsequently, the analysis was performed using a Shimadzu XRD-6100 diffractometer equipped with a copper target. Scanning was carried out over a 2θ range of 10° to 90°, with a step size of 0.02° and a scan speed of 5°/min. The instrument operated at 40 kV and 30 mA.

2.3.9. TG-DTG Analysis

The TG-DTG test was performed to investigate the thermal decomposition characteristics of various mineral phases in the RM-based geopolymers. The powder sample of approximately 5 mg was taken and evenly distributed at the bottom of the alumina crucible. Subsequently, the crucible was placed in the sample chamber of the thermogravimetric analyzer. The analysis was performed with a PerkinElmer Pyris 1 simultaneous thermal analyzer. The test was carried out over a temperature range of 50–800 °C at a heating rate of 10 °C/min, under a N_2 atmosphere.

3. Results and Discussion

3.1. Fresh Properties and Hardened Properties

3.1.1. Flowability

Figure 4 presents the impact of GGBS substitution and the SiO_2/Al_2O_3 ratio on the flowability of RM-based geopolymer slurry. Figure 4(a) that the flowability significantly decreased as the SiO_2/Al_2O_3 ratio increased, with the flow diameter dropping from 165 mm to 125 mm as the ratio rose from 2.25 to 3. This decreased in flowability attributes of the slurry was mainly caused by two principal factors: Firstly, the viscosity of RM-based geopolymer slurry increased with higher SiO_2/Al_2O_3 ratio. Higher viscosity enhanced internal friction between particles, thereby reducing the flowability of the slurry [38]. Secondly, mixtures with higher SiO_2/Al_2O_3 ratios exhibited greater reactivity, promoting the release of more $[SiO_4]^{4-}$ species and the polycondensation of Si–O–Si bonds under alkaline conditions [39]. This led to the formation of a more complex three-dimensional gel network, which reduced the slurry's flowability.

Figure 4(b) demonstrates that the flowability of RM-based geopolymer slurry decreased with increasing GGBS content. When the GGBS content increased from 0.5 to 0.63, the flow diameter was reduced from 155 mm to 130 mm. GGBS exhibits high hydration reactivity. Its particles have relatively smooth surfaces, but the presence of sharp edges on some particles provides more reaction sites, which leads to an increased water demand. Moreover, the high content of reactive species in GGBS led to rapid dissolution in an alkaline environment and facilitated the formation of C-(A)-S-H gels [40]. This process accelerated curing process and reduced the flowability of RM-based geopolymer slurry.

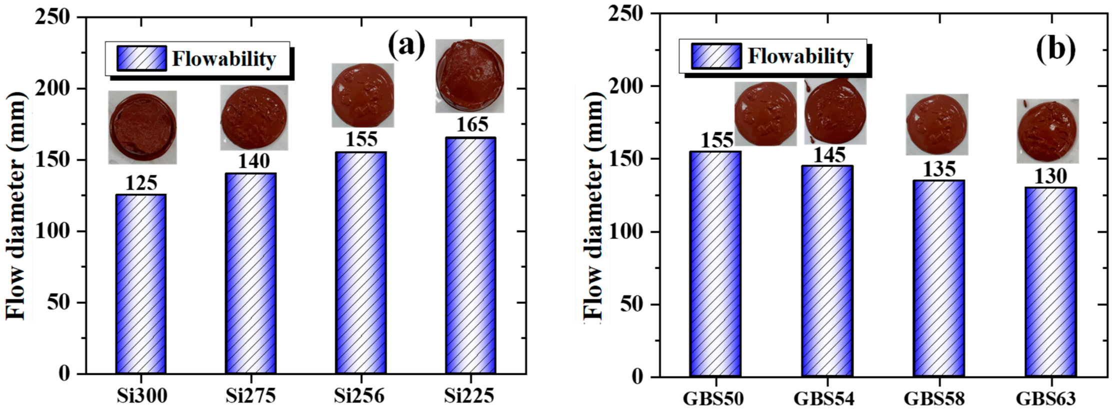

Figure 4. The effect of (a) SiO_2/Al_2O_3 ratio and (b) GGBS on the flowability of RM-based geopolymers.

3.1.2. Setting Time

Figure 5 shows the influence of the SiO_2/Al_2O_3 ratio and GGBS replacement on the setting times of RM-based geopolymers. Figure 5(a) reveals that with fixed ratios of Na_2O/Al_2O_3 and H_2O/Na_2O, increasing the SiO_2/Al_2O_3 ratio from 2.25 to 3 shortened the the initial setting time from 81 to 56 minutes and the final setting time from 102 to 77 minutes. This acceleration was attributed to the higher availability of reactive silicate tetrahedra, which promoted polycondensation reactions and accelerated the formation of the three-dimensional aluminosilicate gel network [29].

Figure 5(b) shows that replacing RM with GGBS also reduced the setting times of RM-based geopolymers. The initial setting time decreased from 72 min to 60 min, and the final setting time was reduced from 95 min to 81 min as the GGBS content increased from 0.5 to 0.63. The results showed that soluble calcium accelerated geopolymer formation [41]. The acceleration resulted from the formation of calcium silicate hydrates gel, which provided nucleation sites and promoted the geopolymerization process [42]. Additionally, the reduction in setting time with increasing GGBS content was also associated with an increase in the SiO_2/Al_2O_3 ratio from 2.56 to 3.12. Therefore, the SiO_2/Al_2O_3 ratio is a key factor governing the setting of geopolymers in both groups.

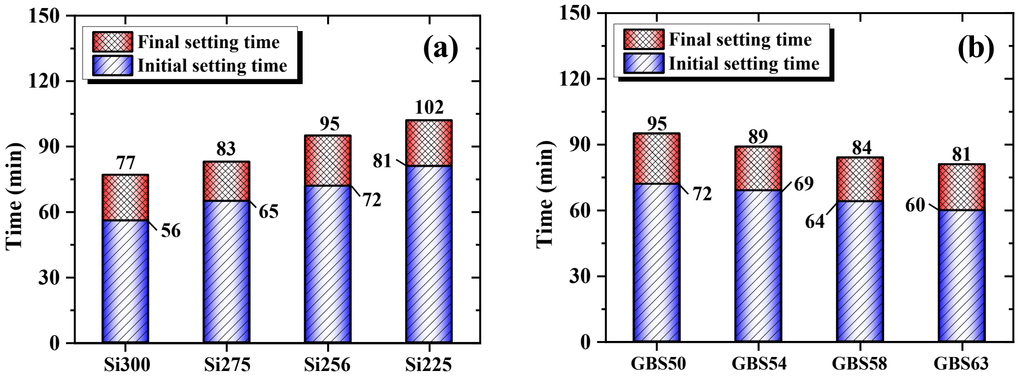

Figure 5. The effect of (a) SiO_2/Al_2O_3 ratio and (b) GGBS on the setting times of RM-based geopolymers.

3.1.3. Compressive Strength

Figure 6 presents the compressive strength of RM-based geopolymers at curing ages of 3, 7, 28, and 56 days. The compressive strength was significantly affected by the SiO_2/Al_2O_3 ratio and GGBS addition. In general, the compressive strength of all geopolymer samples increased with curing age. Figure 6(a) shows that the compressive strength increased significantly as the SiO_2/Al_2O_3 ratio increased from 2.25 to 3. The compressive strength of reference Si225 sample was 44.2 MPa at 56 days. Specifically, the RM-based geopolymers with SiO_2/Al_2O_3 ratios of 2.56, 2.75, and 3.00 exhibited compressive strength increases of 6.3%, 11.3%, and 16.1%, respectively. The polymerization product C-(A)-S-H contributed to the compressive strength development of RM-based geopolymers. As the SiO_2/Al_2O_3 ratio increased, the number of silicate tetrahedra rose, which promoted the formation of more C-(A)-S-H network structures and a denser geopolymer gel phase [43]. Moreover, the SiO_2 dissolution rate enhanced with the increase of the SiO_2/Al_2O_3 ratio in RM-based geopolymers. This may be due to the interference of high concentrations of soluble silicates, which also promoted the dissolution of aluminum [26]. Figure 6(a) also reveals that the development of early compressive strength was significantly governed by the SiO_2/Al_2O_3 ratio. The compressive strength of Si225 was 15.6 MPa at 3 days, while it was 22.7 MPa for Si300.

Figure 6(b) shows that replacing RM with GGBS can improve compressive strength. The compressive strength of RM-based geopolymers with 50% GGBS addition was 47 MPa at 56 days. Compared to the GBS50 sample, the compressive strengths of the GBS54, GBS58, and GBS63 samples increased by 3.2%, 6%, and 8.9%, respectively. This enhancement was due to the granular structure of GGBS and its higher pozzolanic reactivity, which accelerated calcium reactions and resulted in the formation of increased amounts of C-(A)-S-H gel [44]. In addition, the heat generated by the exothermic reaction between GGBS and the alkaline solution promoted the geopolymerization process. This reaction consumed water, enhanced the dissolution of RM and GGBS particles, and increased the alkalinity of the system, thereby accelerating the polycondensation rate [18]. The presence of calcium played a critical role in the early compressive strength development of RM-based geopolymers. The compressive strength of GBS54 and GBS63 samples increased to 17.6 MPa and 20.2 MPa, respectively. This was attributed to the higher pozzolanic reactivity of GGBS compared to RM, and the use of calcium-rich precursors formed additional nucleation sites. Consequently, replacing RM with GGBS promoted more polymerization reactions and product formation, resulting in higher compressive strength of RM-based geopolymers [45].

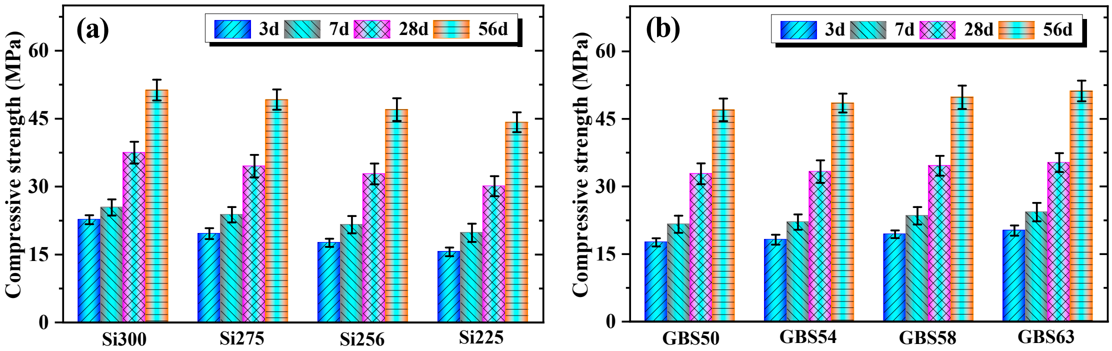

Figure 6. The effect of (a) SiO_2/Al_2O_3 ratio and (b) slag content on the compressive strength of RM-based geopolymers.

3.1.4. Drying Shrinkage

Figure 7 exhibits the impact of the SiO_2/Al_2O_3 ratio and GGBS addition on the drying shrinkage of RM-based geopolymers. Figure 7(a) illustrates that the drying shrinkage rate gradually decreased with an increase in the SiO_2/Al_2O_3 ratio between 2.25 and 3. The drying shrinkage of the Si256, Si275, and Si300 samples decreased by 5.2%, 14.8% and 22.2% compared to the Si225 sample, respectively. Increasing the SiO_2/Al_2O_3 ratio was found to improve the microstructure of RM-based geopolymers, thereby enhancing their resistance to shrinkage. Moreover, the drying shrinkage of geopolymers was primarily influenced by the loss of mesoporous water [46]. The increased ratio of SiO_2/Al_2O_3 can accelerate the hydration process and promote the formation of C-(A)-S-H and N-A-S-H gels, resulting in a denser structure and reduced mesoporosity. Therefore, this reduced the compressive effect of capillary pressure in the mesopores on the gel network and decreased the drying shrinkage of RM-based geopolymers [47].

Figure 7(b) shows the effect of GGBS replacement rate on drying shrinkage. When RM was replaced with GGBS at contents of 54%, 58%, and 63%, the drying shrinkage of RM-based geopolymers was reduced by 5.5%, 10.2% and 14.1%, respectively. This can be attributed to the higher alkaline activation reactivity of GGBS compared to RM. The hydration process was accelerated by the increased GGBS content, leading to changes in the pore structure distribution and porosity of RM-based geopolymers [48]. The crystalline phases in the geopolymer increased stiffness and reduced drying shrinkage. The increase in GGBS replacement rate enhanced the Ca^{2+} concentration in the system, which raised the potential for carbonation of RM-based geopolymers and promoted the formation of more $CaCO_3$ crystals [49]. In addition, the increase in Ca^{2+} content partially accelerated the hydration rate and reduced the evaporation of free water [50].

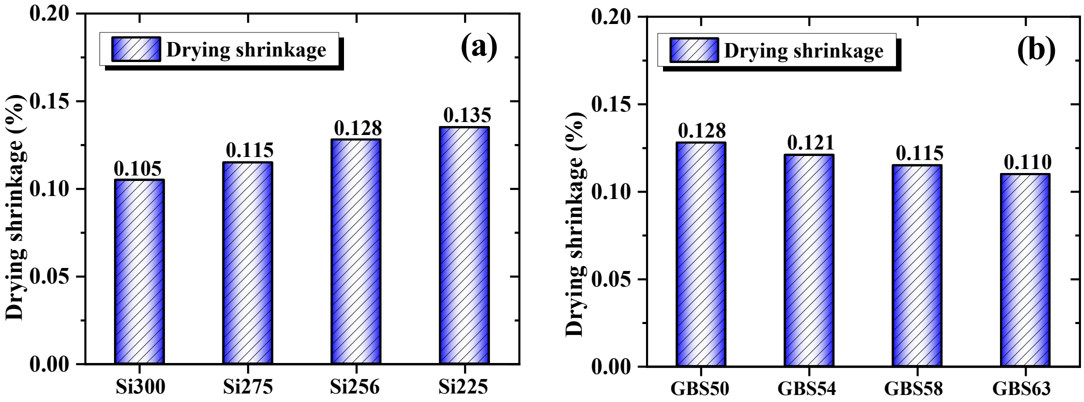

Figure 7. The effect of (a) SiO_2/Al_2O_3 ratio and (b) slag content on the drying shrinkage of RM-based geopolymers.

3.1.5. Water Permeability

Figure 8 illustrates the water permeability results of the geopolymers under varying SiO_2/Al_2O_3 ratios and GGBS content replacing RM. Figure 8(a) shows that the water permeability of RM-based geopolymers decreased as the SiO_2/Al_2O_3 ratio increased from 2.25 to 3. The Si256, Si275, and Si300 samples showed a decrease in water permeability of 5.2%, 9.7%, and 17.2% compared to the Si225 sample, respectively. The reduction in water permeability was attributed to the accelerated formation of C-(A)-S-H gels under higher SiO_2/Al_2O_3 ratios, leading to a more continuous and dense microstructure. This effectively filled the capillary and macropores within the RM-based geopolymers, thereby reducing pore connectivity [43]. Furthermore, the compactness and pore structure of RM-based geopolymers were closely linked to the formation of Si–O–Si bonds [51].The results indicated that increasing the SiO_2/Al_2O_3 ratio facilitated the development of Si–O–Si bonds, thereby enhancing the polymerization process and decreasing the water permeability of RM-based geopolymers.

Figure 8(b) shows that the water permeability of RM-based geopolymers decreased as the GGBS content increased from 50% to 63%. When GGBS was added at 54%, 58% and 63%, it led to decreases of 3.1%, 7.2%, and 11.6% in water permeability, respectively. The reduction in water permeability was closely linked to the microstructure of the geopolymers. This was attributed to the increased Ca^{2+} concentration resulting from the higher GGBS addition, which further facilitated C-(A)-S-H gels formation. These C-(A)-S-H gels possessed a strong filling ability, contributing to a more compact structure of the geopolymer [52]. Moreover, the high reactivity of GGBS under alkaline activation accelerated C-(A)-S-H gel formation. This process consumed the free water in the system and reduced the interconnected porosity formed by water evaporation, thereby decreasing water permeability [53].

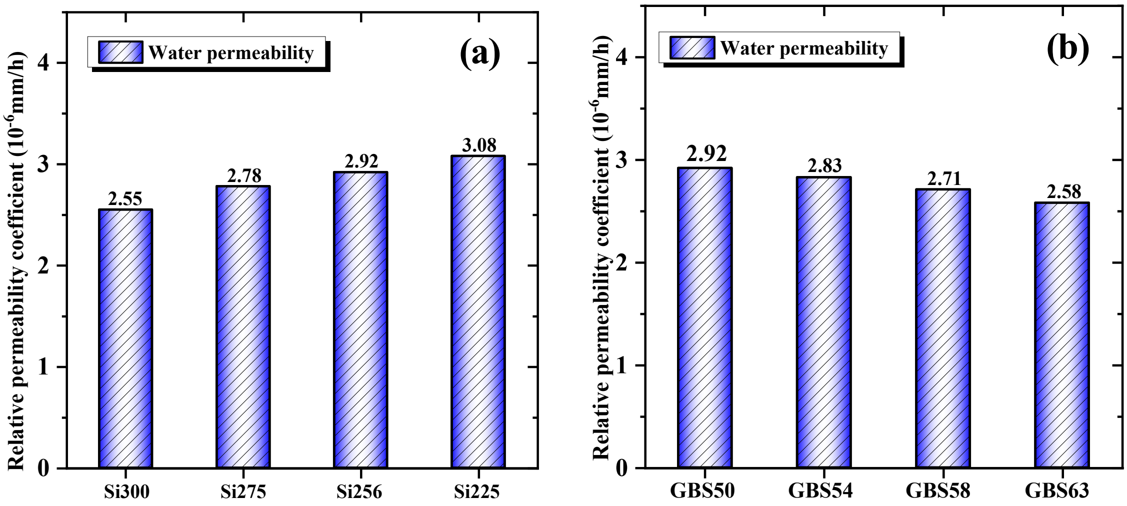

Figure 8. The effect of (a) SiO_2/Al_2O_3 ratio and (b) slag content on the water permeability of RM-based geopolymers.

3.2. Microstructure

In Section 3.1, it was observed that the RM-based geopolymers exhibited optimal performance in terms of setting time, compressive strength, and water permeability when the SiO_2/Al_2O_3 ratio was 3.0. To further explore the influence of varying SiO_2/Al_2O_3 ratios on the hydration characteristics of RM-based geopolymers, this study examines three representative samples—Si225, Si256 (GBS50), and Si300. The aim was to explore how varying SiO_2/Al_2O_3 ratios influence the hydration mechanism and to further clarify the improvement in the properties of RM-based geopolymers under these conditions.

3.2.1. FTIR and XRD Analyses

Figure 9 presents the FTIR spectra of the Si225, Si256, and Si300 samples cured for 28 days. Increasing the SiO_2/Al_2O_3 ratio reduced the absorption peaks around 3445 cm^{-1} and 1641 cm^{-1}, which are associated with the stretching vibrations of O–H bonds and the bending vibrations of H–O–H bonds, respectively. In the Si225 sample, the prominent absorption peaks at 3445 cm^{-1} and 1640 cm^{-1} revealed the presence of significant amounts of adsorbed water and $Ca(OH)_2$ within the system. In contrast, the Si300 sample showed a weakening of these peaks' intensity, indicating that the higher SiO_2/Al_2O_3 ratio promoted the condensation reaction of $[SiO_4]^{4-}$ units. This led to a more efficient consumption of adsorbed water, which was incorporated into the dense C-(A)-S-H gel network, refining the pore structure [54]. The broad peak at around 1423 cm^{-1} was attributed to the stretching vibration of the O-C-O bond in CO_3^{2-}. The CO_3^{2-} peak at 1423 cm^{-1} was more pronounced in Si225 than in Si300. The incomplete incorporation of Ca^{2+} into the C-(A)-S-H gel at lower SiO_2/Al_2O_3 ratios resulted in carbonate formation. Additionally, the RM-based geopolymers may have carbonated due to exposure to air and contact with CO_2. The wide peak at approximately 995 cm^{-1} corresponded to the main asymmetric stretching mode of Si-O-T (T = Si or Al) [55]. As the SiO_2/Al_2O_3 ratio increased from 2.25 to 3, the Si-O-T absorption peak shifted from 991 cm^{-1} to 999 cm^{-1}, indicating an enhancement in the polymerization degree of the aluminosilicate network in RM-based geopolymers. This facilitated the development of a dense gel structure mainly controlled by Si–O–Si bonds [56]. Furthermore, a higher SiO_2/Al_2O_3 ratio caused an increase in the wavenumber of the Si–O vibrational absorption peak around 480 cm^{-1}. These findings indicated that the FT-IR spectra of all the samples exhibited similarities, and there may be variations in the crystallinity of the materials in the amorphous regions.

Figure 9 shows the XRD pattern of Si225, Si256, and Si300 samples cured for 28 days. The identified components included C-(A)-S-H, N-A-S-H, quartz, calcite, hematite, hydrotalcite and calcium hydroxide [57]. In the Si225 sample, the quartz peak exhibited a relatively high intensity in the 20°–40° range, indicating incomplete reaction of the siliceous materials due to the low SiO_2/Al_2O_3 ratio. Additionally, the characteristic peaks of calcite and calcium hydroxide were observed at 29.25° and 49.75°, respectively. This was because calcium ions were not fully incorporated into the C-(A)-S-H gel network. The formation of calcite and calcium hydroxide through carbonation or hydration resulted in a more porous and less compact structure. In contrast, the Si300 sample exhibited a significant reduction in the intensities of the quartz, calcite and calcium hydroxide peaks. The intensity of the broad amorphous peak corresponding to C-(A)-S-H and N-A-S-H enhanced between 20° and 35°. The intensity of the characteristic peak for hydrotalcite decreased at 24.45°. This indicated that the silicate-driven condensation reaction promoted the formation of a dense amorphous gel phase, with a higher degree of Ca^{2+} involvement in the development of the C-(A)-S-H gel network [58]. The study revealed that higher SiO_2/Al_2O_3 ratios resulted in denser gel network formation, which enhanced the compressive strength of RM-based geopolymers.

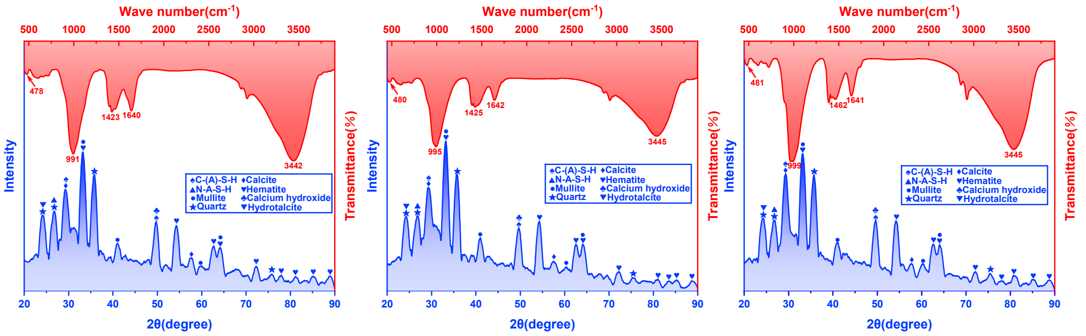

(a) Si225 (b) Si256 (c) Si300

Figure 9. FTIR and XRD curves of RM-based geopolymers cured for 28days: (a) Si225; (b) Si256; (c) Si300.

3.2.2. TG-DTG Analysis

Figure 10 shows the TG-DTG curves of the Si225, Si256, and Si300 samples cured for 28 days. The TG-DTG curves revealed four distinct weight loss processes within the temperature range of 50°C to 800°C. The peak observed between 89.17°C and 162.34°C was primarily attributed to the dehydration of C-(A)-S-H or ettringite (AFt) in the hydration product [59]. This peak corresponded to the formation of hydration products, with varying SiO_2/Al_2O_3 ratios in C-(A)-S-H leading to a wide range of dehydration temperatures. The second weight loss process, observed between 218.67°C and 347.51°C, was caused by the decomposition of $Al(OH)_3$ or hydrotalcite. The third and fourth weight loss stages took place between 414.84°C and 535.35°C, and 614.84°C and 735.52°C, respectively. The absorption peak between 414.84°C and 535.35°C was primarily caused by the dehydration and decomposition of $Ca(OH)_2$ [60]. The temperature range of 614.84°C–735.52°C was attributed to the decarbonation of carbonate minerals such as $CaCO_3$, which formed during the carbonation of $Ca(OH)_2$ in the curing process [61]. Compared to the Si225 and Si256 samples, the Si300 sample released a greater amount of amorphous gel at 28 days. This phenomenon was reflected in the weight loss of the hydration product C-(A)-S-H-bound water, with absorption peaks occurring between 89.17°C and 162.34°C. The increase in gel formation was attributed to the higher SiO_2/Al_2O_3 ratio, which promoted the formation of C-(A)-S-H. Moreover, the RM exhibited low activity, and the addition of GGBS increased the concentration of Ca^{2+}, which reacted with $[SiO_4]^{4-}$, $[AlO_4]^{4-}$, and CO_3^{2-} monomers to generate C-(A)-S-H gels and $CaCO_3$ crystals, thereby improving the compressive strength of the composite [62]. In general, the increase in the SiO_2/Al_2O_3 ratio resulted in a higher quantity of hydration products and a denser gel network, which in turn reduced moisture adsorption in the pores. These findings were consistent with the drying shrinkage and water permeability analysis.

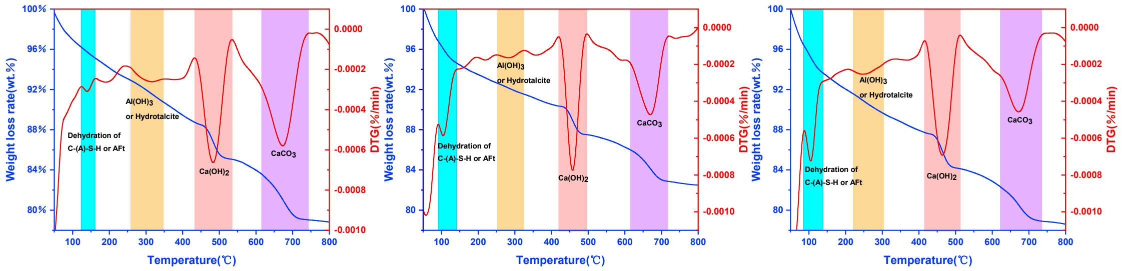

(a) Si225 (b) Si256 (c) Si300

Figure 10. TG-DTG curves of RM-based geopolymers cured for 28days: (a) Si225; (b) Si256; (c) Si300.

3.2.3. SEM-EDS Analysis

Figure 11 shows the SEM-EDS images of the Si225, Si256, and Si300 samples at 28 days. The SiO_2/Al_2O_3 ratio influenced the quantity of hydration products and the microstructural density in RM-based geopolymers. In the Si225 sample, $CaCO_3$ and $Ca(OH)_2$ crystals were embedded within the loosely interwoven C-(A)-S-H gel network. The surface of the Si225 sample exhibited extensive long cracks and large pores, which contributed to a loosely structured matrix and reduced mechanical properties. When the SiO_2/Al_2O_3 ratio increased, the C-(A)-S-H gel formed a dense microstructure through highly polymerized silicate tetrahedra. The crystals of $CaCO_3$ and $Ca(OH)_2$ were embedded into the C-(A)-S-H gel, leading to shortened crack lengths, reduced pore size and decreased pore quantity, which enhanced the microstructural density of RM-based geopolymers. This phenomenon was attributed to the increased SiO_2/Al_2O_3 ratio, which promoted the polycondensation rate of silicate ions in an alkaline environment [63]. This promoted C-(A)-S-H gel formation and the precipitation and crystallization of Ca^{2+} with CO_3^{2-}/OH^-, leading to the development of a gel-crystal interpenetrating network structure [64]. In addition, the amount of C-(A)-S-H in the hydration products increased with a higher SiO_2/Al_2O_3 ratio, which significantly improved pore filling and crack repair, leading to a densified structure with high compressive strength.

The EDS analysis of the Si225, Si256, and Si300 samples confirmed that the surface compositions were predominantly composed of Fe, Ca, Si, Al, and Na. The spots 1–3 located on the surface of the C-(A)-S-H gels exhibited Ca/Si ratios from 1.02 to 1.43 and Si/Al ratios between 1.58 and 1.68. Specifically, the Ca/Si ratio for Si300 was 1.43, compared to 1.02 for Si225. The Si/Al ratio for Si300 was 1.68, while for Si225, it was 1.62. The results indicate that higher Ca/Si and Si/Al ratios in C-(A)-S-H gels typically correspond to a highly cross-linked three-dimensional structure. Therefore, it can be concluded that increasing the SiO_2/Al_2O_3 ratio promoted the polymerization degree of the C-(A)-S-H gel network, leading to a denser microstructure and enhancing the compressive strength of RM-based geopolymers.

Preprints.org (www.preprints.org) | NOT PEER-REVIEWED | Posted: 11 July 2025 doi:10.20944/preprints202507.0800.v1

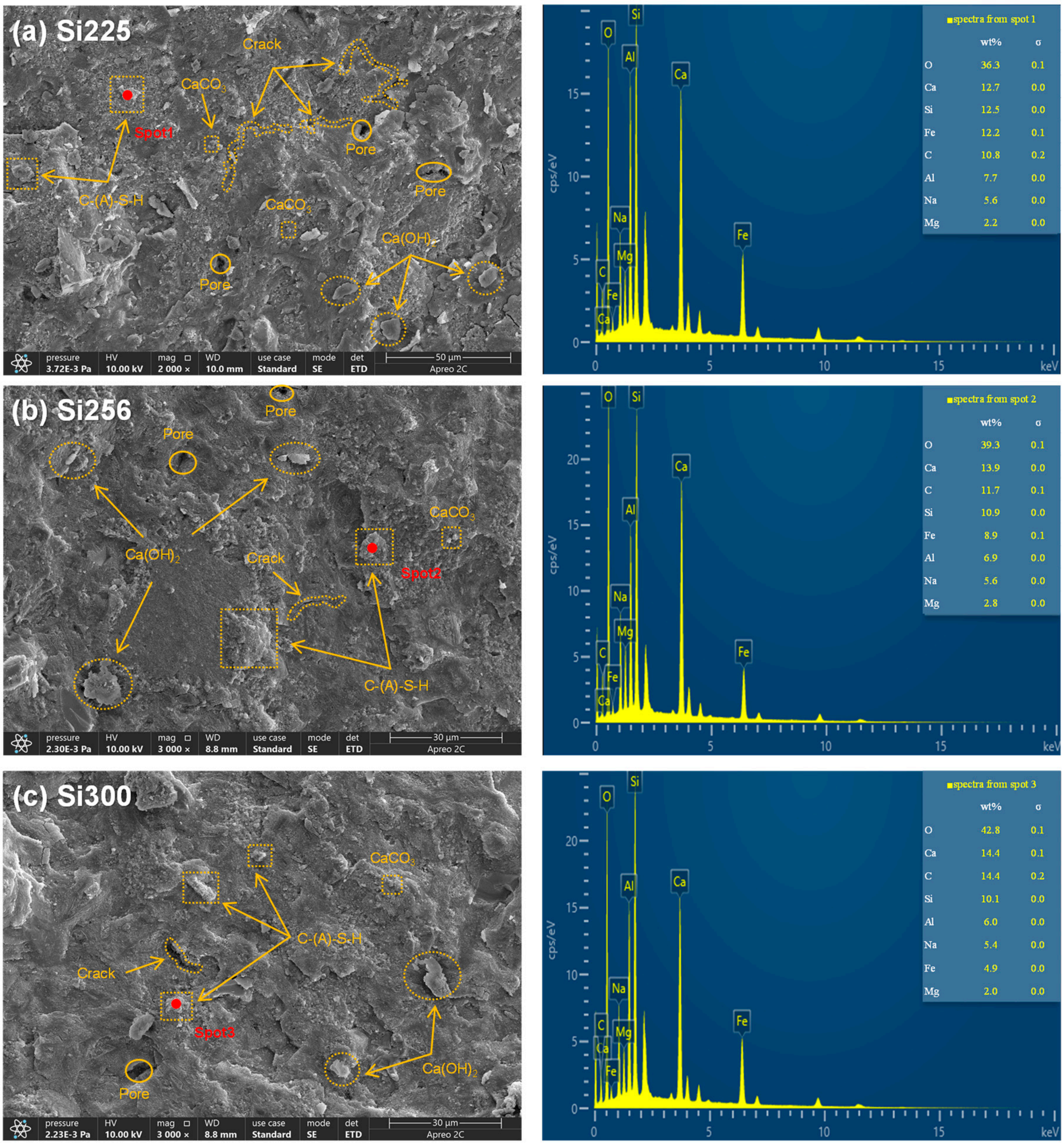

spectra from spot 1

	wt%	σ
O	36.3	0.1
Ca	12.7	0.0
Si	12.5	0.0
Fe	12.2	0.1
C	10.8	0.2
Al	7.7	0.0
Na	5.6	0.0
Mg	2.2	0.0

spectra from spot 2

	wt%	σ
O	39.3	0.1
Ca	13.9	0.0
C	11.7	0.1
Si	10.9	0.0
Fe	8.9	0.1
Al	6.9	0.0
Na	5.6	0.0
Mg	2.8	0.0

spectra from spot 3

	wt%	σ
O	42.8	0.1
Ca	14.4	0.1
C	14.4	0.2
Si	10.1	0.0
Al	6.0	0.0
Na	5.4	0.0
Fe	4.9	0.0
Mg	2.0	0.0

Figure 11. SEM-EDS images of RM-based geopolymers cured for 28days: (a) Si225; (b) Si256; (c) Si300.

3.3. Sustainability Analysis

The carbon emissions and costs generated in the experiment mainly arise from the production and transportation of materials. The raw material cost and carbon emission data used in this study were sourced from previous research [59,64–67]. Table 3 lists the CO_2 emissions and costs for each raw material. RM exhibited considerably higher CO_2 emissions compared to GGBS, and NaOH released significantly more CO_2 than $Na_2O{\cdot}nSiO_2$. The GGBS and $Na_2O{\cdot}nSiO_2$ contributed substantial amounts of SiO_2 to the geopolymer system. Increasing the SiO_2/Al_2O_3 ratio enhanced the compressive strength and reduced CO_2 emissions. Furthermore, GGBS was more expensive than RM, indicating that its use may increase the cost of geopolymers. Therefore, optimizing the GGBS replacement rate was necessary [68].

In order to assess the sustainability impact of RM-based geopolymers, Table 4 compares the cost and CO_2 emissions of samples with different SiO_2/Al_2O_3 ratios to those of geopolymers containing RM and GGBS. The RM-based geopolymers with similar compressive strengths showed unit volume CO_2 emissions and cost ranging from 327.53–347.62 kg/m^3 and 881.3–1162.04 CNY/kg, respectively. Compared to the reference RM-based geopol[59,64–67ymers, the CO_2 emissions and costs were reduced by 13.13%–44.33% and 3.64%–39.68%, respectively [69–71]. This further illustrated their synergistic contribution to sustainability. The CO_2 emissions of RM-based geopolymers first decreased and then increased as the SiO_2/Al_2O_3 ratio increased from 2.25 to 3. In the range of SiO_2/Al_2O_3 ratios between 2.25 and 2.56, the reduction in CO_2 emissions was primarily attributed to the decreased consumption of RM and NaOH. However, when the SiO_2/Al_2O_3 ratio exceeded 2.56, achieving a higher ratio required a substantial increase in the quantities of GGBS and Na2O·nSiO2. The results indicated that an appropriate increase in the SiO_2/Al_2O_3 ratio promoted the densification of the aluminosilicate network, enhanced mechanical properties and reduced CO_2 emissions. This effectively improved compressive strength with environmental and economic outcomes.

Table 3. CO_2 emissions and costs of each constituent of RM-based geopolymers.

Material type	CO_2 emissions (kg CO_2•eq/kg)	Cost [a] (CNY/kg)
RM [59,64]	0.303	0.22
GGBS [59,65]	0.067	0.5
NaOH [59,65]	3.2	7.53
$Na_2O·nSiO_2$ [b] [59,66]	0.4	4.67
Water [c] [67]	0	0.0083

a Market price may fluctuate. b Sodium silicate mentioned here refers to the solid content of the solution, excluding water. c Water includes the additional water added and the water in the activators.

Table 4. CO_2 emissions and costs of RM-based geopolymers per unit volume.

type	Mixtures in references			Mixtures in this study			
	[69]	[70]	[71]	Si225	Si256	Si275	Si300
RM (kg/m^3)	714.05	519.56	471.05	613.00	551.40	484.83	413.31
GGBS (kg/m^3)	714.05	779.35	706.57	481.64	551.40	642.68	734.78
NaOH (kg/m^3)	95.25	58.45	52.99	33.93	28.67	36.08	40.18
$Na_2O·nSiO_2$ (kg/m^3)	48.41	55.20	101.28	52.54	79.40	77.80	84.96
Water (kg/m^3)	428.43	487.09	500.49	569.21	551.40	541.21	528.12
CO_2 emissions (kg/m^3)	588.38	418.77	400.16	347.62	327.53	336.54	337.03
Cost (CNY/kg)	1461.03	1205.96	1333.07	881.30	988.30	1019.21	1162.04
Compressive strength (28, MPa)	36	34	37	30.1	32.8	34.5	37.5
CO_2 intensity (kg/m^3/MPa)	16.34	12.32	10.82	11.55	9.99	9.75	8.99
Cost intensity (CNY/m^3/MPa)	40.58	35.47	36.03	29.28	30.13	29.54	30.99

4. Conclusions

In this study, the fresh and hardened properties, along with the microstructural characteristics of RM-based geopolymers prepared with varying SiO_2/Al_2O_3 ratios and GGBS replacement rates were investigated. In addition, the environmental and economic effects were assessed for geopolymers with different SiO_2/Al_2O_3 ratios. Based on the experimental results and discussions, the conclusions derived from the findings were as follows:

(1) The high SiO_2/Al_2O_3 ratio and increased GGBS addition raised the concentrations of SiO_2 and Ca^{2+} in the system, respectively. This accelerated the formation of a three-dimensional gel network, resulting in reduced setting time and flowability of RM-based geopolymers.

(2) Increasing the SiO_2/Al_2O_3 ratio and GGBS addition enhanced the 56-day compressive strength by 6.3–16.1% and 3.2–8.9%, respectively. The higher SiO_2/Al_2O_3 ratio increased the concentration of $[SiO_4]^{4-}$ units and facilitated the dissolution of Si and Al. GGBS promoted the release of Ca^{2+} and exothermic reactions, thereby improving the strength of RM-based geopolymers.

(3) When the SiO_2/Al_2O_3 ratio increased, drying shrinkage was reduced by 22.2% due to the enhanced formation of C-(A)-S-H/N-A-S-H gels and a decrease in mesopore content. High GGBS addition reduced the shrinkage by 14.1%, primarily promoting C-(A)-S-H gels formation, facilitating $CaCO_3$ crystallization and reducing the evaporation of free water. Both approaches reduced water permeability by optimizing the pore structure and enhancing the densification of the gel network.

(4) The primary hydration products of RM-based geopolymers included C-(A)-S-H, N-A-S-H, calcite, hydrotalcite and calcium hydroxide. These products effectively filled the pores, leading to a more compact microstructure. SEM-EDS analysis further showed that raising the SiO_2/Al_2O_3 ratio reduced crack length and pore quantity. $CaCO_3$, $Ca(OH)_2$ and C-(A)-S-H formed an interpenetrating gel-crystal network structure. The Ca/Si ratio in the C-(A)-S-H gel increased from 1.02 to 1.43, and the Si/Al ratio rose from 1.62 to 1.68.

(5) In comparison to the referenced RM-based geopolymers, the CO_2 emission and costs in this study were reduced by 13.13%–44.33% and 3.64%–39.68%, respectively. The CO_2 emissions of RM-based geopolymers were closely influenced by the SiO_2/Al_2O_3 ratio. Adjusting the SiO_2/Al_2O_3 ratio effectively reduced CO_2 emissions, thereby promoting sustainability.

Acknowledgements: This work was financially supported by the National Natural Science Foundation of China (Grant No. 52368046), State Key Laboratory of Safety and Resilience of Civil Engineering in Mountain Area (Grant No. HJGZ2024205), and the Key Research and Development Program of Jiangxi Province in China (Grant Nos. 20240N006, 20224BAB204074).

References

1. Y. Zhao, Y. Zheng, J. He, K. Cui, P. Shen, G. Peng, R. Guo, D. Xia, C.S. Poon, Production of carbonates calcined clay cement composites via CO2-assisted vigorous stirring, Cement and Concrete Composites **2025**, 163, 106181. https://doi.org/10.1016/j.cemconcomp.2025.106181
2. Z. Li, H.F. Dong, X.S. Zhao, K. Wang, X.J. Gao, Utilization of bayer red mud for high-performance geopolymers: competitive roles of different activators, Case Stud. Constr. Mater. **2025**. https://doi.org/10.2139/ssrn.5252244.
3. M.T. Ghafoor, N. Rakhimova, C. Shi, One part geopolymers: A comprehensive review of advances and key challenges, J. Build. Eng. **2025**, 111, 113112. https://doi.org/10.1016/j.jobe.2025.113112
4. A. Hassan, C. Zhang, Dynamic and static behaviour of geopolymer concrete for sustainable infrastructure development: Prospects, challenges, and performance review, Compos. Struct. **2025**, 359, 118984. https://doi.org/10.1016/j.compstruct.2025.118984
5. K. Guo, H. Dong, J. Zhang, L. Zhang, Z. Li, Experimental study of Alkali-Activated cementitious materials using thermally activated red mud: Effect of the Si/Al ratio on fresh and mechanical properties, Buildings, **2025**, 15(4), 565. https://doi.org/10.3390/buildings15040565
6. X. Jiang, R. Xiao, M.M. Zhang, W. Hu, Y. Bai, B.S. Huang, A laboratory investigation of steel to fly ash-based geopolymer paste bonding behavior after exposure to elevated temperatures. Construction and Building Materials. **2020**. https://doi.org/10.1016/j.conbuildmat.2020.119267
7. S. Karthik, K. Saravana Raja Mohan, G. Murali, S.R. Abid, S. Dixit, Impact of various fibers on mode I, III and I/III fracture toughness in slag, fly Ash, and silica fume-based geopolymer concrete using edge-notched disc bend specimen, Theor. Appl. Fract. Mech. **2024**, 134, 104751. https://doi.org/10.1016/j.tafmec.2024.104751
8. H. Bilal, T.F. Chen, M. Ren, X.J. Gao, A.S. Su: Influence of silica fume, metakaolin & sbr latex on strength and durability performance of pervious concrete. Construction and Building Materials, 275. **2021**. https://doi.org/10.1016/j.conbuildmat.2020.122124
9. E.A. Abdelrahman, Y.G. Abou El-Reash, H.M. Youssef, Y.H. Kotp, R.M. Hegazey, Utilization of rice husk and waste aluminum cans for the synthesis of some nanosized zeolite, zeolite/zeolite, and geopolymer/zeolite products for the efficient removal of Co(II), Cu(II), and Zn(II) ions from aqueous media, J. Hazard. Mater. **2021**, 401, 123813. https://doi.org/10.1016/j.jhazmat.2020.123813

10. J. Zhao, A. Wang, Y. Zhu, J. Dai, Q. Xu, K. Liu, F. Hao, D. Sun, Manufacturing ultra-high performance geopolymer concrete (UHPGC) with activated coal gangue for both binder and aggregate, Composites Part B: Engineering **2024**, 284, 111723. https://doi.org/10.1016/j.compositesb.2024.111723
11. Y.S. Wudil, A. Al-Fakih, M.A. Al-Osta, M.A. Gondal, Intelligent optimization for modeling carbon dioxide footprint in fly ash geopolymer concrete: A novel approach for minimizing CO2 emissions, J. Environ. Chem. Eng. **2024**, 12(1), 111835. https://doi.org/10.1016/j.jece.2023.111835
12. L. Qin, X.J. Gao, Properties of coal gangue-portland cement mixture with carbonation. Fuel. **2019**. https://doi.org/10.1016/j.fuel.2019.02.067
13. X. Liu, Y. Han, F. He, P. Gao, S. Yuan, Characteristic, hazard and iron recovery technology of red mud - a critical review, J. Hazard. Mater. **2021**, 420, 126542. https://doi.org/10.1016/j.jhazmat.2021.126542
14. Y. Li, X. Min, Y. Ke, D. Liu, C. Tang, Preparation of red mud-based geopolymer materials from MSWI fly ash and red mud by mechanical activation, Waste Manage. **2019**, 83, 202-208. https://doi.org/10.1016/j.wasman.2018.11.019
15. U. Zakira, K. Zheng, N. Xie, B. Birgisson, Development of high-strength geopolymers from red mud and blast furnace slag, J. Clean. Prod. **2023**, 383, 135439. https://doi.org/10.1016/j.jclepro.2022.135439
16. Y. Liu, Y. Zhuge, X. Chen, W. Duan, R. Fan, L. Outhred, L. Wang, Micro-chemomechanical properties of red mud binder and its effect on concrete, Composites Part B: Engineering **2023**, 258, 110688. https://doi.org/10.1016/j.compositesb.2023.110688
17. T. Qin, H. Luo, R. Han, Y. Zhao, L. Chen, M. Liu, Z. Gui, J. Xing, D. Chen, B. He, Red mud in combination with construction waste red bricks for the preparation of Low-Carbon binder materials: Design and material characterization, Buildings, **2024**, 14(12), 3982. https://doi.org/10.3390/buildings14123982
18. U. Zakira, K. Zheng, N. Xie, B. Birgisson, Development of high-strength geopolymers from red mud and blast furnace slag, J. Clean. Prod. **2023**, 383, 135439. https://doi.org/10.1016/j.jclepro.2022.135439
19. K. Tian, Y. Wang, B. Dong, G. Fang, F. Xing, Engineering and micro-properties of alkali-activated slag pastes with Bayer red mud, Constr. Build. Mater. **2022**, 351, 128869. https://doi.org/10.1016/j.conbuildmat.2022.128869
20. I.M. Nikbin, M. Aliaghazadeh, Sh Charkhtab, A. Fathollahpour, Environmental impacts and mechanical properties of lightweight concrete containing bauxite residue (red mud), J. Clean. Prod. **2018**, 172, 2683-2694. https://doi.org/10.1016/j.jclepro.2017.11.143
21. Z. Luo, M. Ge, L. Liu, X. Liu, W. Zhang, J. Ye, M. Gao, Y. Yang, M. Zhang, X. Liu, Desulfurization-modified red mud for supersulfated cement production: Insights into hydration kinetics, microstructure, and mechanical properties, Composites Part B: Engineering **2025**, 297, 112340. https://doi.org/10.1016/j.compositesb.2025.112340
22. Y. Tan, X. Zhang, Z. Liu, F. Wang, S. Hu, Dealkalization behavior and leaching mechanisms of red mud with simulated aluminum profile wastewater, Dev. Built Environ. **2025**, 21, 100613. https://doi.org/10.1016/j.dibe.2025.100613
23. X. Xi, K.A. Jin, X. Niu, S. Zhang, A novel tandem pyrolysis-catalytic upgrading strategy for plastic waste to high-value products with zeolite and red mud, Energy **2025**, 330, 136921. https://doi.org/10.1016/j.energy.2025.136921
24. X. Li, S. Jin, T. Yan, X. Qiao, J. Yuan, Unraveling the interactive effects of Na2O/Al2O3, SiO2/Al2O3 and calcium on the properties of geopolymers from circulating fluidized bed fly ashes, Case Stud. Constr. Mater. **2024**, 21, e3798. https://doi.org/10.1016/j.cscm.2024.e03798
25. M. Irfan Khan, K. Azizli, S. Sufian, Z. Man, Sodium silicate-free geopolymers as coating materials: Effects of Na/Al and water/solid ratios on adhesion strength, Ceram. **2015**, 41 (2, Part B), 2794-2805. https://doi.org/10.1016/j.ceramint.2014.10.099
26. B. Kim, J. Kang, Y. Shin, T. Yeo, J. Heo, W. Um, Effect of Si/Al molar ratio and curing temperatures on the immobilization of radioactive borate waste in metakaolin-based geopolymer waste form, J. Hazard. Mater. **2023**, 458, 131884. https://doi.org/10.1016/j.jhazmat.2023.131884
27. L. Zheng, W. Wang, Y. Shi, The effects of alkaline dosage and Si/Al ratio on the immobilization of heavy metals in municipal solid waste incineration fly ash-based geopolymer, Chemosphere **2010**, 79(6), 665-671. https://doi.org/10.1016/j.chemosphere.2010.02.018

28. Z. Li, J. Zhang, Z. Lei, M. Gao, J. Sun, L. Tong, S. Chen, Y. Wang, Designing low-carbon fly ash based geopolymer with red mud and blast furnace slag wastes: Performance, microstructure and mechanism, J. Environ. Manage. **2024**, 354, 120362. https://doi.org/10.1016/j.jenvman.2024.120362
29. J. Liu, J. Doh, D.E.L. Ong, H.L. Dinh, Z. Podolsky, G. Zi, Investigation on red mud and fly ash-based geopolymer: Quantification of reactive aluminosilicate and derivation of effective Si/Al molar ratio, J. Build. Eng. **2023**, 71, 106559. https://doi.org/10.1016/j.jobe.2023.106559
30. M. Rowles, B. O'Connor, Chemical optimisation of the compressive strength of aluminosilicate geopolymers synthesised by sodium silicate activation of metakaolinite, Journal of Materials Chemistry **2003**, 13(5), 1161-1165. https://doi.org/10.1039/B212629J
31. G. Kim, S. Cho, S. Im, J. Yoon, H. Suh, M. Kanematsu, A. Machida, T. Shobu, S. Bae, Evaluation of the thermal stability of metakaolin-based geopolymers according to Si/Al ratio and sodium activator, Cement and Concrete Composites **2024**, 150, 105562. https://doi.org/10.1016/j.cemconcomp.2024.105562
32. K. Pimraksa, P. Chindaprasirt, A. Rungchet, K. Sagoe-Crentsil, T. Sato, Lightweight geopolymer made of highly porous siliceous materials with various Na2O/Al2O3 and SiO2/Al2O3 ratios, Materials Science and Engineering: A **2011**, 528(21), 6616-6623. https://doi.org/10.1016/j.msea.2011.04.044
33. P. Duxson, A. Fernández-Jiménez, J.L. Provis, G.C. Lukey, A. Palomo, J.S.J. van Deventer, Geopolymer technology: The current state of the art, J. Mater. Sci. **2007**, 42(9), 2917-2933. https://doi.org/10.1007/s10853-006-0637-z
34. F. Souayfan, E. Roziere, C. Justino, M. Paris, D. Deneele, A. Loukili, Comprehensive study on the reactivity and mechanical properties of alkali-activated metakaolin at high H2O/Na2O ratios, Appl. Clay Sci. **2023**, 231, 106758. https://doi.org/10.1016/j.clay.2022.106758
35. D. Khale, R. Chaudhary, Mechanism of geopolymerization and factors influencing its development: A review, J. Mater. Sci. **2007**, 42 (3), 729-746. https://doi.org/10.1007/s10853-006-0401-4
36. G. Saini, U. Vattipalli, Assessing properties of alkali activated GGBS based self-compacting geopolymer concrete using nano-silica, Case Stud. Constr. Mater. **2020**, 12, e352. https://doi.org/10.1016/j.cscm.2020.e00352
37. X. Zhou, Z. Geng, J. Shi, Enhanced passivity of reinforcing steel in cementitious materials with thermally-activated red mud, Cement and Concrete Composites **2024**, 153, 105696. https://doi.org/10.1016/j.cemconcomp.2024.105696
38. K. Kopecskó, M. Hajdu, A.A. Khalaf, I. Merta, Fresh and hardened properties for a wide range of geopolymer binders – an optimization process, Cleaner Engineering and Technology **2024**, 21, 100770. https://doi.org/10.1016/j.clet.2024.100770
39. R. Churata, J. Almirón, M. Vargas, D. Tupayachy-Quispe, J. Torres-Almirón, Y. Ortiz-Valdivia, F. Velasco, Study of geopolymer composites based on volcanic ash, fly ash, pozzolan, metakaolin and mining tailing, Buildings, **2022**, 12(8), 1118, https://doi.org/10.3390/buildings12081118
40. H. El-Hassan, P. Kianmehr, D. Tavakoli, A. El-Mir, R.S. Dehkordi, Synergic effect of recycled aggregates, waste glass, and slag on the properties of pervious concrete, Dev. Built Environ. **2023**, 15, 100189. https://doi.org/10.1016/j.dibe.2023.100189
41. D. Hou, D. Wu, X. Wang, S. Gao, R. Yu, M. Li, P. Wang, Y. Wang, Sustainable use of red mud in ultra-high performance concrete (UHPC): Design and performance evaluation, Cement and Concrete Composites **2021**, 115, 103862. https://doi.org/10.1016/j.cemconcomp.2020.103862
42. Y.H. Emminger, L. Ladner, C. Ruiz-Agudo, Comparative study of the early stages of crystallization of calcium silicate hydrate (C-S-H) and calcium aluminate silicate hydrate (C-A-S-H), Cem. Concr. Res. **2025**, 193, 107873. https://doi.org/10.1016/j.cemconres.2025.107873
43. X. Chen, Z. Niu, J. Wang, G.R. Zhu, M. Zhou, Effect of sodium polyacrylate on mechanical properties and microstructure of metakaolin-based geopolymer with different SiO2/Al2O3 ratio, Ceram. **2018**, 44(15), 18173-18180. https://doi.org/10.1016/j.ceramint.2018.07.025
44. J. Xie, J. Wang, R. Rao, C. Wang, C. Fang, Effects of combined usage of GGBS and fly ash on workability and mechanical properties of alkali activated geopolymer concrete with recycled aggregate, Composites Part B: Engineering **2019**, 164, 179-190. https://doi.org/10.1016/j.compositesb.2018.11.067

45. T. Ai, D. Zhong, Y. Zhang, J. Zong, X. Yan, Y. Niu, The Effect of Red Mud Content on the Compressive Strength of Geopolymers under Different Curing Systems, Buildings, **2021**, 11(7), 298, https://doi.org/10.3390/buildings11070298
46. Z. Yang, Z. Chen, H. Zhu, B. Zhang, Z. Dong, X. Zhan, Efficient utilization of coral waste for internal curing material to prepare eco-friendly marine geopolymer concrete, J. Environ. Manage. **2024**, 368, 122173. https://doi.org/10.1016/j.jenvman.2024.122173
47. Z. Liu, C. Gao, H. Rong, S. Liu, Y. Shi, H. Wang, Q. Wang, X. Zhang, J. Han, K. Jing, H. Wu, X. Chen, K. Deng, The shrinkage and durability performance evaluations for concrete exposed to temperature variation environments at early-age, J. Build. Eng. **2025**, 104, 112457. https://doi.org/10.1016/j.jobe.2025.112457
48. M. Feng, C. Jiang, Y. Wang, Y. Zou, J. Zhao, Experimental study on mechanical properties and drying shrinkage compensation of solidified Ultra-Fine dredged sand blocks made with GGBS-Based geopolymer, Buildings, **2023**, 13(7), 1750, https://doi.org/10.3390/buildings13071750
49. W. Chen, H. Zhu, Y. Li, L. Yang, S. Cheng, H. Yu, Engineered cementitious composites using blended limestone calcined clay and fly ash: Mechanical properties and drying shrinkage modeling, Case Stud. Constr. Mater. **2024**, 20, e2960. https://doi.org/10.1016/j.cscm.2024.e02960
50. P. Wang, Z.Y. Yin, P.Y. Hicher, Y.J. Cui, Micro-mechanical analysis of one-dimensional compression of clay with dem. International Journal for Numerical and Analytical Methods in Geomechanics. **2023**, 47. https://doi.org/10.1002/nag.3597
51. A. Hajimohammadi, J.L. Provis, J.S.J. van Deventer, The effect of silica availability on the mechanism of geopolymerisation, Cem. Concr. Res. **2011**, 41(3), 210-216. https://doi.org/10.1016/j.cemconres.2011.02.001
52. M.P. Bilondi, M.A. Daluee, M. Amirriahi, M.A. Eslamieh, K. Rajaee, M. Zaresefat, Durability assessment of clay soils stabilised with geopolymers based on recycled glass powder in various corrosive environments, Results Eng. **2025**, 27, 105691. https://doi.org/10.1016/j.rineng.2025.105691
53. S.X. Song, P. Wang, Z.Y. Yin, Y. P. Cheng, Micromechanical modeling of hollow cylinder torsional shear test on sand using discrete element method. Journal of Rock Mechanics and Geotechnical Engineering. **2024**, 16. https://doi.org/10.1016/j.jrmge.2024.02.010
54. M. Zhang, M. He, Z. Pan, Inhibition of efflorescence for fly ash-slag-steel slag based geopolymer: Pore network optimization and free alkali stabilization, Ceram. **2024**, 50 (22, Part C), 48538-48550. https://doi.org/10.1016/j.ceramint.2024.09.202
55. Z. Hu, M. Wyrzykowski, P. Lura, Estimation of reaction kinetics of geopolymers at early ages, Cem. Concr. Res. **2020**, 129, 105971. https://doi.org/10.1016/j.cemconres.2020.105971
56. A. Raza, A. Selmi, K.M. Elhadi, N. Ghazouani, W. Chen, Strength analysis and microstructural characterization of calcined red mud based-geopolymer concrete modified with slag and phosphogypsum, Journal of Materials Research and Technology **2024**, 33, 6168-6181. https://doi.org/10.1016/j.jmrt.2024.10.248
57. T. Ai, D. Zhong, Y. Zhang, J. Zong, X. Yan, Y. Niu, The Effect of Red Mud Content on the Compressive Strength of Geopolymers under Different Curing Systems. Buildings, **2021**, 11(7), 298, https://doi.org/10.3390/buildings11070298
58. A.M. Gaifutdinov, K.A. Andrianova, L.M. Amirova, R.R. Amirov, Optimizing the manufacturing technology of high-strength fiber reinforced composites based on aluminophosphates, Composites Part A: Applied Science and Manufacturing **2024**, 185, 108310. https://doi.org/10.1016/j.compositesa.2024.108310
59. Z. Li, M. Gao, Z. Lei, L. Tong, J. Sun, Y. Wang, X. Wang, X. Jiang, Ternary cementless composite based on red mud, ultra-fine fly ash, and GGBS: Synergistic utilization and geopolymerization mechanism, Case Stud. Constr. Mater. **2023**, 19, e2410. https://doi.org/10.1016/j.cscm.2023.e02410
60. Y. Chen, C. Zou, C.L. Yong, R.J.S. Jan, T.H. Tan, J. Lin, K.H. Mo, Utilization of waste glass as precursor material in one-part alkali-activated aggregates, Journal of Materials Research and Technology **2024**, 33, 5551-5558. https://doi.org/10.1016/j.jmrt.2024.10.204
61. Z. Yang, R. Li, H. Zhu, B. Zhang, Z. Dong, X. Zhan, G. Zhang, H. Zhang, Synthesis of eco-sustainable seawater sea-sand geopolymer mortars from ternary solid waste: Influence of microstructure evolution on mechanical performance, Sustain. Mater. Technol. **2024**, 41, e1056. https://doi.org/10.1016/j.susmat.2024.e01056

62. R. Cioffi, L. Maffucci, L. Santoro, Optimization of geopolymer synthesis by calcination and polycondensation of a kaolinitic residue, Resources, Conservation and Recycling **2003**, 40(1), 27-38. https://doi.org/10.1016/S0921-3449(03)00023-5
63. L.M. Costa, T.D.C.C. Souza, R.K.F.G. Oliveira, N.G.S. Almeida, M. Houmard, Effects of silicas and aluminosilicate synthesized by sol-gel process on the structural properties of metakaolin-based geopolymers, Appl. Clay Sci. **2025**, 267, 107743. https://doi.org/10.1016/j.clay.2025.107743
64. K. Chen, W. Lin, Q. Liu, B. Chen, V.W.Y. Tam, Micro-characterizations and geopolymerization mechanism of ternary cementless composite with reactive ultra-fine fly ash, red mud and recycled powder, Constr. Build. Mater. **2022**, 343, 128091. https://doi.org/10.1016/j.conbuildmat.2022.128091
65. B. Lyu, L. Guo, X. Fei, J. Wu, R. Bian, Preparation and properties of green high ductility geopolymer composites incorporating recycled fine brick aggregate, Cement and Concrete Composites **2023**, 139, 105054. https://doi.org/10.1016/j.cemconcomp.2023.105054
66. M. He, Z. Yang, N. Li, X. Zhu, B. Fu, Z. Ou, Strength, microstructure, CO2 emission and economic analyses of low concentration phosphoric acid-activated fly ash geopolymer, Constr. Build. Mater. **2023**, 374, 130920. https://doi.org/10.1016/j.conbuildmat.2023.130920
67. L. Qin, X.J. Gao, Q.Y. Li, Upcycling carbon dioxide to improve mechanical strength of portland cement. Journal of Cleaner Production. **2018**. https://doi.org/10.1016/j.jclepro.2018.06.120
68. H. Bahmani, H. Mostafaei, P. Santos, N. Fallah Chamasemani, Enhancing the mechanical properties of Ultra-High-Performance concrete (UHPC) through silica sand replacement with steel slag, Buildings, **2024**, 14(11), 3520, https://doi.org/10.3390/buildings14113520
69. Z. Sun, Q. Tang, B.S. Xakalashe, X. Fan, M. Gan, X. Chen, Z. Ji, X. Huang, B. Friedrich, Mechanical and environmental characteristics of red mud geopolymers, Constr. Build. Mater. **2022**, 321, 125564. https://doi.org/10.1016/j.conbuildmat.2021.125564
70. A. Bayat, A. Hassani, O. And Azami, Thermo- mechanical properties of alkali-activated slag–Red mud concrete, Road Mater. Pavement Des. **2020**, 21 (2), 411-433. https://doi.org/10.1080/14680629.2018.1500299
71. A. Bayat, A. Hassani, A.A. Yousefi, Effects of red mud on the properties of fresh and hardened alkali-activated slag paste and mortar, Constr. Build. Mater. **2018**, 167, 775-790. https://doi.org/10.1016/j.conbuildmat.2018.02.105